scientific reports

Check for updates

OPEN

Inorganic cesium lead mixed halide based perovskite solar materials modified with functional silver iodide

Vincent Obiozo Eze[1], Lucas Braga Carani[1], Haimanti Majumder[2], M. Jasim Uddin[2]✉ & Okenwa I. Okoli[1]✉

Inorganic $CsPbIBr_2$ perovskites have recently attracted enormous attention as a viable alternative material for optoelectronic applications due to their higher efficiency, thermal stability, suitable bandgap, and proper optical absorption. However, the $CsPbIBr_2$ perovskite films fabricated using a one-step deposition technique is usually comprised of small grain size with a large number of grain boundaries and compositional defects. In this work, silver iodide (AgI) will be incorporated as an additive into the $CsPbIBr_2$ perovskite precursor solution to prepare the unique perovskite $CsI(PbBr_2)_{1-x}(AgI)_x$. The AgI additive in the precursor solution works as a nucleation promoter which will help the perovskite to grow and merge into a continuous film with reduced defects. With detailed characterizations, we found that incorporating AgI additive resulted in a uniform perovskite film with fewer grain boundaries, increased grain size, crystallinity, optical absorption while decreasing carrier recombination and trap density. Using the AgI in an optimum amount, we fabricated $CsPbIBr_2$ perovskite solar cells (PSCs) with a simple structure and achieved a power conversion efficiency (PCE) of 7.2% with a reduced hysteresis index. This work offers an alternative approach towards preparing high-quality $CsPbIBr_2$ perovskite films for solar cells with higher stability and other optoelectronic applications.

Organic–inorganic metal halide perovskites are considered promising materials for potential applications in photovoltaics (PV), photodetectors, light-emitting diodes, and other optoelectronic applications[1–4]. The reason behind this vast applicability is their excellent optoelectronic properties, such as strong optical absorption, small exciton binding energy, large diffusion length, and ambipolar charge mobility[5–9]. The basic formula of organic–inorganic hybrid perovskite is ABX_3, where A and B are organic/inorganic cation, and X is an anion. Currently, the power conversion efficiency (PCE) of perovskite solar cells (PSCs) have soared up to 25.5%[10–13], rivaling that of the commercial crystalline silicon, cadmium telluride (CdTe), and copper indium gallium selenide (CIGS) thin-film solar cells[14,15]. Despite the meteoric rise in the PCEs of the organic–inorganic-based PSCs, it is still dealing with the problem of poor thermal stability. Moreover, significant decomposition after annealing methylammonium lead halide ($MAPbI_3$) perovskite at 85 °C resulting in phase separation of $MAPbI_3$ into PbI_2 and MAI has been widely reported[16–18].

Recently, all inorganic cesium metal halide perovskites ($CsPbI_xBr_{3-x}$ ($x = 0–3$)) have attracted considerable attention as a rising light harvester due to their superior thermal stability over the widely used organic–inorganic metal halide perovskites, as well as their potential for use in PSCs and other optoelectronic devices[19–22]. However, the PCE of $CsPbI_xBr_{3-x}$ based PSCs is still not as high as the organic–inorganic lead halide perovskites. This can be attributed to poor film quality with defects and trap sites that resulted in a low short circuit current and poor phase stability[23,24]. Among the inorganic $CsPbI_xBr_{3-x}$ based perovskites, $CsPbBr_3$ demonstrates superior stability under environmental stresses[25–27] but has a large bandgap of about 2.3 eV, which is not ideal for solar cell applications. The $CsPbI_3$, and $CsPbI_2Br$ exhibit comparatively narrow bandgaps of about 1.73 and 1.92 eV, respectively, but their thermal stability markedly deteriorates when they are exposed to high environmental stress like moisture, heat, ultraviolet radiation, etc. Interestingly, the $CsPbIBr_2$ perovskite have balanced features, such as

[1]High-Performance Materials Institute, FAMU-FSU College of Engineering, 2525 Pottsdamer Street, Tallahassee, FL 32310, USA. [2]Photonics and Energy Research Lab, Department of Chemistry, University of Texas Rio Grande Valley, 1201 W University Drive, Edinburg, TX 78539, USA. ✉email: mohammed.uddin@utrgv.edu; okoli@eng.famu.fsu.edu

a bandgap of 2.05 eV and phase stability which makes it the most promising materials for optoelectronic devices. Although the poor film quality of the one-step solution-processed $CsPbIBr_2$ perovskite hinders optimization of the device performance, additive engineering that involves the metal ion doping approach has been proven to be an effective strategy to improve the surface morphology, crystallinity, and photophysical properties and reduce the defects of $CsPbI_xBr_{3-x}$ perovskites[22,28]. This method is one of the most facile perovskite film preparation methods and plays a significant role in creating homogenous nucleation sites to enhance the crystallization rate, enlarging crystals to some extent, and modifying the surface energy to control the crystal growth directions of the perovskite[11,29–34]. To date, metal ions, such as Mn^{2+}[30,35], Bi^{3+}[36], Li^{+}[37], Sr^{2+}[16], Zn^{2+}[38], Eu^{2+}[39], Ni^{2+}[11] Ba^{2+}[28] have been incorporated into the perovskite crystal lattice to achieve improved films.

Zhao et al. used Sn^{2+} doping in $CsPbIBr_2$ based PSCs and achieved a PCE of 11.33%[40]. The high PCE achieved by the Sn^{2+} doped PSCs was speculated to result from high short-circuit density (J_{sc}) due to broadened light response range rather than decreased grain boundaries and compositional defect densities in the intrinsic $CsPbIBr_2$ perovskite film[37]. In recent studies, it has been demonstrated that by using a preheating assisted spin-coating method, light processing, intermolecular exchange, interface passivation, and the combination of additive and anti-solvent dripping approach, the compositional defects of the $CsPbIBr_2$ perovskite devices can be suppressed, and its PCE[15,25,41–43] is increased. Although the above-mentioned methods are more efficient $CsPbIBr_2$ PSCs, their approaches may be difficult to reproduce due to the multiple complex steps of perovskite film preparation. Therefore, it became essential to develop a simple and structured way to prepare uniform and high-quality $CsPbIBr_2$ perovskite films that exhibit large grains, fewer grain boundaries, low defects density. Shahbazi et al. successfully modified the lattice structure to considerably improve the crystallinity, morphology, electronic properties of organic–inorganic hybrid perovskites ($CH_3NH_3PbI_3$), as well as device performance using AgI additive[44]. However, the influence of AgI additive on $CsPbI_xBr_{3-x}$ perovskites for a photovoltaic application has not been investigated.

Herein, we prepared AgI modified $CsPbIBr_2$ perovskite films using a simple, one-step solution process. The influence of AgI additive on the structural, morphological, optical, and electronic properties of the $CsPbIBr_2$ perovskite film was systematically investigated by examining different characterizations. We observed that the AgI additive markedly improved the surface coverage, grain size, crystallinity, and photophysical properties of the perovskite film. The AgI additive has also improved charge extraction and reduced the defect density in the perovskite film, as well as improved the solar cell's performance. We fabricated PSCs using a ubiquitous structure to assess the effect of AgI additive on the device performance. The best-performing device achieved a PCE of 7.20% with a reduced hysteresis index. Our study provides a novel and facile strategy for morphology and crystallization controls and reduces defects in the $CsPbIBr_2$ perovskite films for fabricating efficient PSCs and other optoelectronic devices.

Materials and methods

Materials and reagent. Fluorine-doped tin oxide (FTO) glass substrates (sheet resistance: 12–15 Ω/sq.) were purchased from MSE supplies. Liquid detergent (Hellemanex), Titanium (IV) Chloride (TiCl4, Alfa Aesar). All other chemicals were purchased from Sigma Aldrich and were used as received.

Device fabrication. The patterned FTO-coated glass substrates were used, an electron transporting layer (ETL, compact TiO_2) was prepared as reported elsewhere[45,46]. The $CsPbIBr_2$ perovskite films were prepared by mixing CsI (1 M) and $PbBr_2$ (1 M) in dimethyl sulfoxide (DMSO) (1 ml) in a nitrogen-filled glovebox and spin-coated on top of the compact TiO_2/FTO substrates at 1500 rpm for 45s[22]. The perovskite films were prepared with AgI in mass percentages with respect to $PbBr_2$ as the pristine perovskite[22,44]. The perovskite films were thermally annealed at 70 °C for 2 min, followed by 280 °C for 10 min. The hole transport layer (HTL, Spiro-OMeTAD) was prepared as reported elsewhere[45–49]. The contact electrode was deposited by thermal evaporation of Au metal with a thickness of 100 nm at 3.4×10^{-4} Pa. The solar cells' active areas were 0.06 cm^2.

Materials and device characterization. The morphology and particle size of the perovskite films were determined using scanning electron microscopy (SEM). SEM images were taken by a high-resolution field emission scanning electron microscope (FESEM) (JEOL 7401F). The crystalline structures of the as-prepared materials were characterized by powder X-ray diffraction (XRD) pattern (Scintag Pad-V, XRD powder diffractometer, graphite monochromatic Cu Kα radiation). The X-ray photoemission spectroscopy (XPS) was performed with an Mg Kα (1253.6 eV) X-ray source (Perkin Elmer). The absorption spectra of the films were measured using an ultraviolet–visible (UV–vis) spectrophotometer (Agilent Varian Cary 5000). The current density–voltage (*J–V)* measurements of the PSCs were recorded on a Keithley 2400 source measurement unit, IV5 solar cell I-V measurement system (PV Measurements, Inc.) under a simulated AM 1.5G illumination (Newport Oriel Instrument U.S.A, 94022A). Incident photon-to-electron conversion efficiency (IPCE) measurements were performed using light from the 300 W xenon lamp passed through a cornerstone 260 monochromator (Newport, 74,125) onto the cells, and the light scanned from 300 to 800 nm in 5 nm intervals. Incident light intensity and photocurrent were measured using a power meter (Newport, 2936-C) and Oriel 71580 Silicon Detector Head (Newport).

Results and discussion

The functional AgI nanoparticles was incorporated in different mass fractions (1.0, 2.0, 5.0%) into the precursor solution with respect to $PbBr_2$ to prepare the $CsI(PbBr_2)_{1-x}(AgI)_x$ perovskite films[22,44]. The photograph of the precursor solution with and without AgI additive is shown in Fig. S1. It was observed that the introduction of AgI led to the color change of the $CsPbIBr_2$ perovskite precursor, suggesting the successful incorporation of the additive. For effective comparison, pure $CsPbIBr_2$ perovskite films were also prepared. Both the $CsPbIBr_2$

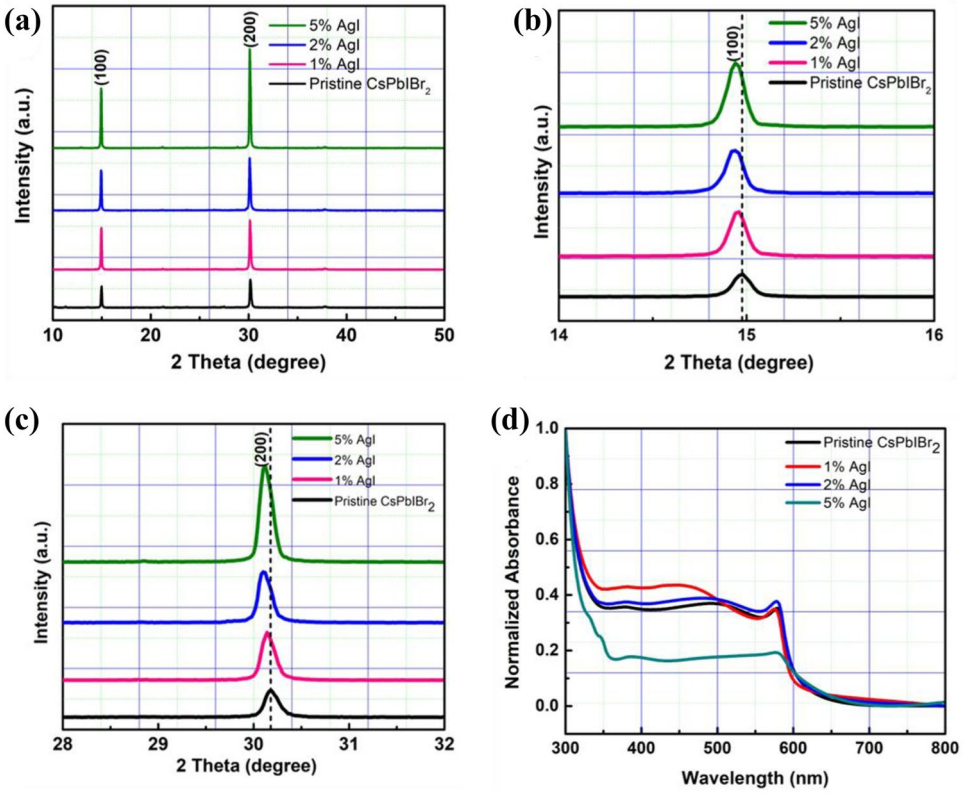

Figure 1. (**a**) XRD pattern of $CsPbIBr_2$ perovskite films with and without AgI doping. (**b**) (100) peaks shift of the perovskite films. (**c**) (200) peaks shift of the perovskite films. (**d**) UV–vis spectra of with and without AgI doping.

(without AgI doping) and the $CsI(PbBr_2)_{1-x}(AgI)_x$ perovskite films were prepared by spin-coating with solutions containing cesium iodide (CsI) and lead bromide ($PbBr_2$) in DMSO on top of a c-TiO_2/FTO substrate. XRD characterization was performed to examine the influence of AgI on the crystallization of $CsPbIBr_2$ perovskite films. Figure 1a shows the XRD pattern of the corresponding $CsPbIBr_2$ perovskite films with different amounts of AgI. The main diffraction peaks around 14.93° and 30.16° can be assigned to the lattice plane of (100) and (200) of the α-phase perovskite[11,30]. The perovskite thin films showed no characteristic diffraction peaks of Ag in the bulk of the $CsI(PbBr_2)_{1-x}(AgI)_x$ perovskite due to the smaller amount[22,50,51]. By comparison, the diffraction intensity of $CsI(PbBr_2)_{1-x}(AgI)_x$ perovskite films increased and the full width at half maximum (fwhm) decreased with the increasing amount of AgI additive, indicating improved crystallinity of the perovskites[34,52]. We estimated the average crystallite sizes using the Scherrer's equation described below:

$$D = \frac{K\lambda}{\beta cos\theta} \tag{1}$$

where D is the average crystallite size (nm), λ is the wavelength (nm) of the X-rays, β is the fwhm (radian) of the diffraction peak, θ is the diffraction angle (degree), and K (0.94) is the shape factor. It can be observed that the crystallite sizes of the with AgI perovskite films are larger than the without AgI perovskite film, as shown in Fig. S2. This further confirms improved crystallinity for the AgI-doped perovskite films, which is advantageous in enhancing the optoelectronic properties of the perovskite films and device efficiency. The shifts in peak position were further investigated by analyzing the (100) and (200) peaks, as shown in Fig. 1b,c. The positions of the (100) and (200) XRD diffraction peaks shifted to a lower degree as the concentration of the AgI increased. This indicates an enlarged crystal lattice due to Ag doping while simultaneously showing that the Ag ions participate in the lattice formation[11,38]. Figure 1d shows the optical absorption spectra of the pristine $CsPbIBr_2$ and AgI-doped $CsPbIBr_2$ perovskite films. Note that conditions for all the fabricated films were the same except for the AgI doping concentration. Notably, an enhanced optical absorption was observed for the 1% and 2% AgI doped $CsPbIBr_2$ perovskite films. The absorption seems to be reduced when the amount of AgI increases to 5%. Figure 2a shows the optical bandgap of the perovskite films calculated from the Tauc plot. The bandgap was increased for the AgI doped $CsPbIBr_2$ perovskites, suggesting that the presence of the AgI dopants slightly modified the interactions with the ions in the network, leading to changes in the bandgap[53]. The XPS analysis was performed to identify the existence of AgI in $CsPbIBr_2$ perovskite films. The survey scans for the binding energies from 0 to 1000 eV clearly showed the signals of Cs, Pb, I, Br, and C for both doped and undoped perovskite films (Fig. 2b). Figure 2c shows that Ag had been incorporated into the $CsPbIBr_2$ perovskite. The peak intensities of Ag $3d_{3/2}$ and Ag $3d_{5/2}$ were observed to increase with the Ag content, which affirms the successful incorporation of AgI into

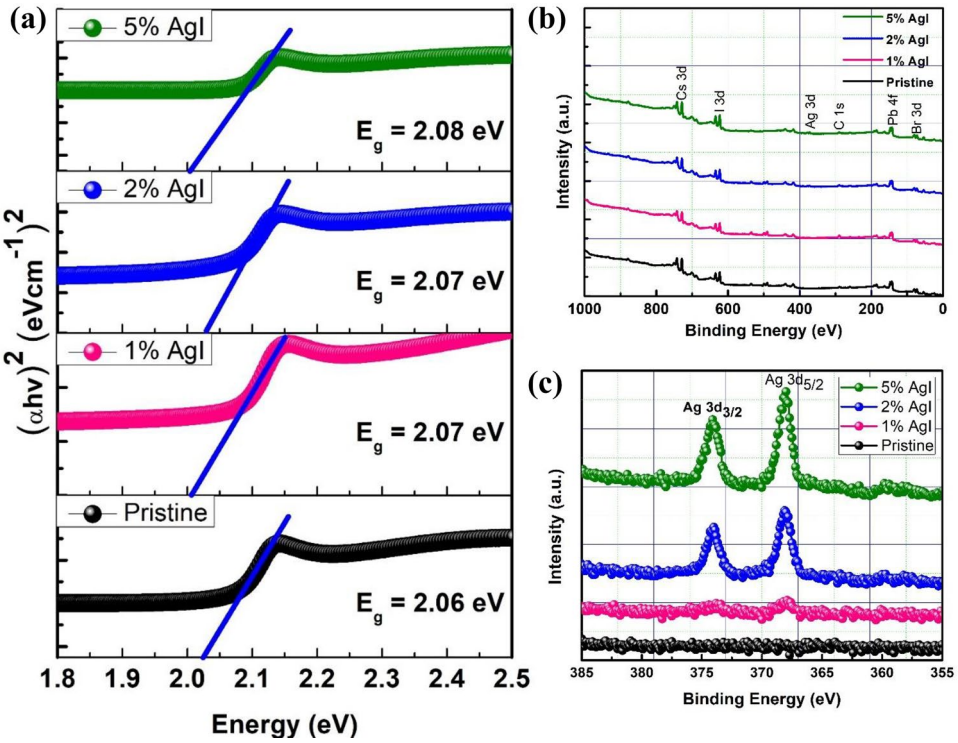

Figure 2. (**a**) Tauc plots of $CsPbIBr_2$ perovskite films with and without AgI doping. XPS results for undoped and AgI doped $CsPbIBr_2$ perovskite films. (**b**) Survey scan, (**c**) Ag 3d XPS spectra of undoped and AgI doped $CsPbIBr_2$ perovskites.

the perovskite material[50,54]. Figure S3 shows the high-resolution spectra for Cs, Pb, I and Br. In comparison to the pristine sample, no apparent changes in the binding energy position for the AgI-doped $CsPbIBr_2$ perovskite composition were observed, owing to the small substitution ratio of AgI[40].

To examine the changes in the morphology of $CsPbIBr_2$ perovskite films and the influence of Ag doping in controlling the crystal growth, we compared the SEM images of both doped and non-doped perovskite films. Figure 3a–d shows the SEM images of the pure and AgI based $CsPbIBr_2$ perovskite films. Figure 3a shows that the $CsPbIBr_2$ perovskite film exhibited a non-uniform morphology with voids on its surface. Previously reported work has suggested that the formation of such voids is probably due to the extremely slow crystallization of $CsPbIBr_2$, where $CsPbIBr_2$ species will crystallize from the precursor film containing plenty of DMSO molecules and then shrinks to leave behind isolated voids[22,25]. Interestingly, when 1% AgI is incorporated into the $CsPbIBr_2$ perovskite, the morphology of the $CsPbIBr_2$ perovskites showed marked changes.

Large, uniform grains developing in marked pin-hole free films were observed in Fig. 3b. The 1% AgI perovskite film exhibited a compact and uniform morphology with larger grain size and fewer grain boundaries. These properties are expected to decrease the crystal defects and trap density while also reducing charge recombination and enhancing charge transport in the device[22,45–47,55–57]. Upon increasing the amount of AgI to 2% (Fig. 3c), the grain size was further enlarged, with the largest grains resulting from the 5% AgI dopant (Fig. 3d). However, we also observed that 2% and 5% AgI perovskite films showed wrinkles and wave-like features, which can be attributed to defects caused by excess AgI in the perovskite host[52]. Recently, we reported the possible mechanism for improving surface coverage for the $CsI(PbBr_2)_{1-x}(AgI)_x$ perovskite films, as shown in Fig. 2 [22]. Ag islands were formed for the precursor solution containing AgI additive upon depositing it on a substrate. The Ag seeds could act as crystal growth promoters for the perovskite to grow and merge into a continuous film with fewer grain boundaries and enhanced crystallinity[22,52,54,58]. To examine the impact of AgI doping on the device performance, a simple and ubiquitous planar PSCs based on FTO/c-TiO_2/$CsI(PbBr_2)_{1-x}(AgI)_x$/Spiro-OMeTAD/Au geometry was fabricated as presented in Fig. 4a. Table 1 summarizes the PV parameters of PSCs based on $CsPbIBr_2$ perovskite films with and without AgI doping. Figure 4b shows the *J-V* characteristics of the AgI additive modified $CsPbIBr_2$ and the pristine PSCs. The pristine device delivered a PCE of 5.2% (average value 4.50%) with a J_{sc} of 10.29 mA/cm^2, a V_{oc} of 0.88 V, and *FF* of 0.57. The reason behind the lower efficiency of the pristine $CsPbIBr_2$ PSC is poor perovskite film quality (see Fig. 4a). Moreover, insufficient coverage could facilitate a high frequency of shunt paths and allow contact between the electron transport layer (ETL) and hole transporting layer (HTL), thereby decreasing the PV parameters of the PSCs[48,56,59,60]. The 1% AgI doped device yielded the highest PCE of 7.2% (average value 6.85%) with a J_{sc} of 11.00 mA/cm^2, a V_{oc} of 0.92 V, and a FF of 0.71, which are higher than the pristine device. It was noticed that with an increasing amount of the concentration of AgI doping beyond 2% led to a decrease in the PV performance. The higher PCE achieved by the 1% AgI doped device demonstrates that Ag doping plays an important role in efficiency enhancement due to the improved surface morphology,

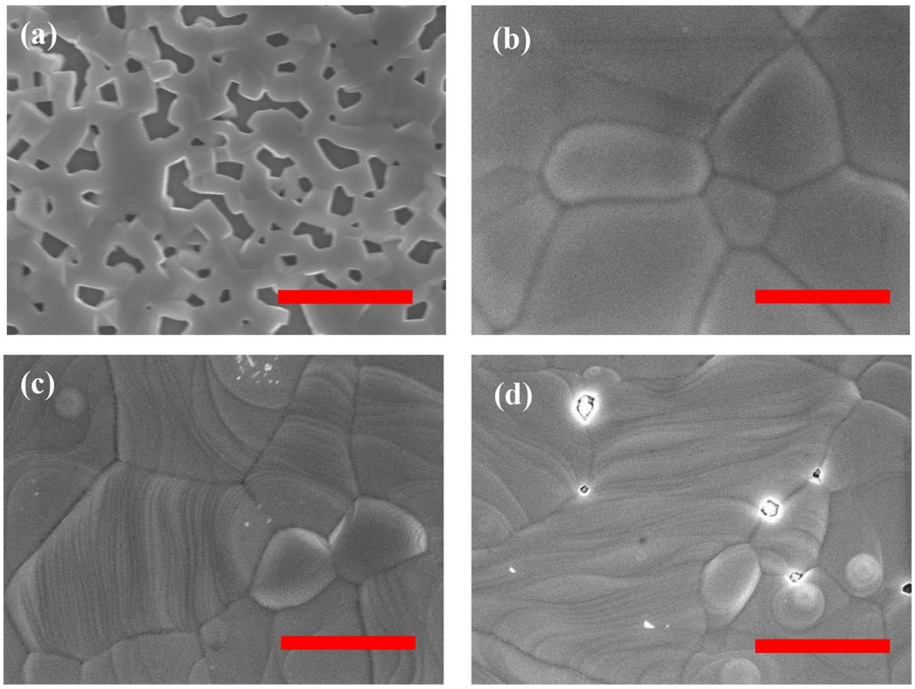

Figure 3. Low and high magnification SEM images of (**a**,**b**) pristine perovskite, (**c**,**d**) 1% AgI, (**e**,**f**) 2% AgI, (**g**,**h**) 5% AgI. Scale bars is 1 μm.

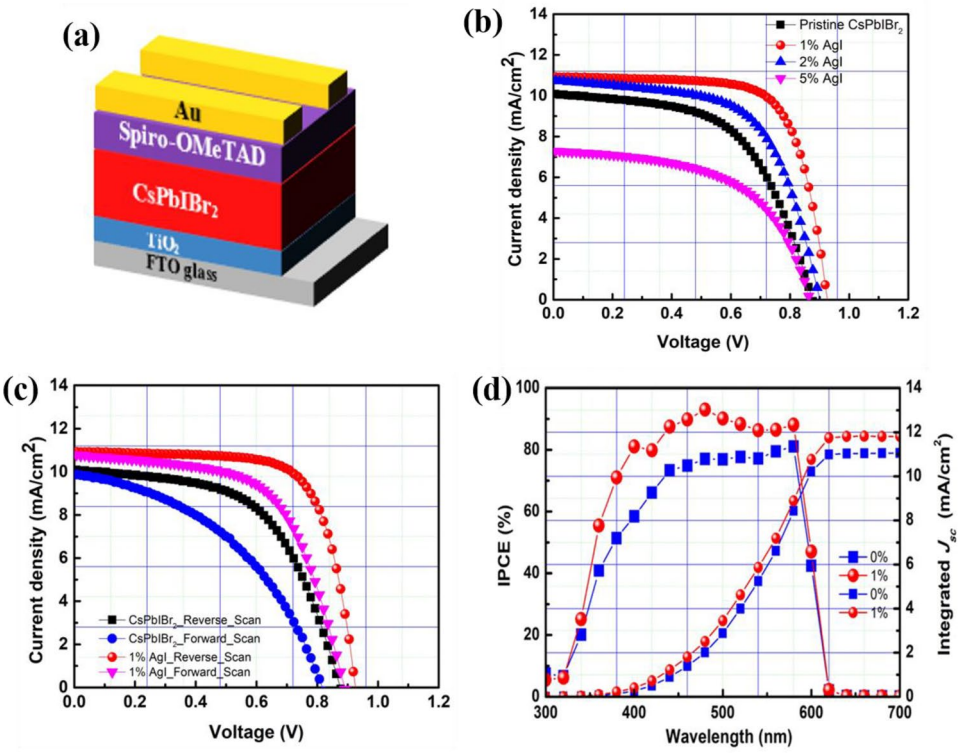

Figure 4. (**a**) Schematic diagram of the device architecture (**b**) Reserve scan of J-V curves for $CsPbIBr_2$ perovskite PSCs with and without AgI incorporation measured under simulated AM 1.5 G illumination (**c**) Hysteresis behavior of pristine and 1% AgI $CsPbIBr_2$ PSCs. (**d**) IPCE of the devices.

Device	J_{sc} (mA/cm^2)	Voc (V)	FF	PCE (%)	Average PCE (%)
Pristine	10.29	0.88	0.57	5.2	4.50 ± 0.4
1% AgI	11.00	0.92	0.71	7.2	6.85 ± 0.2
2% AgI	10.94	0.90	0.61	6.0	5.72 ± 0.2
5% AgI	7.39	0.86	0.58	3.7	1.16 ± 0.7

Table 1. Summary of PV parameters of the best performing devices together with the average PCE of the pristine and AgI based $CsPbIBr_2$ PSCs measured under standard AM 1.5G illumination with a light intensity of 100 mW/cm^2.

crystallinity, enlarged grain size, and fewer grain boundaries and defects. Figure 4c shows the forward scan (from a short circuit to an open circuit) and reverse scan (from an open circuit to a short circuit) for the pristine and 1% AgI doped $CsPbIBr_2$ PSCs. Anomalous hysteresis of *J-V* measurements has been widely reported as one of the most critical issues in PSCs, which often gives rise to the overestimation of the solar's PCE. Typically, the origin of hysteresis can be from the charge-selective layers, trapping and de-trapping of charge carriers, ionic movement, or ferroelectric properties of the perovskite materials[47–49,61–65]. It is apparent that both devices showed hysteresis in *J-V* curves scanned in the reverse and forward direction. According to our experimental results, the additive AgI does not alleviate the hysteresis behavior in the PSCs; however, the hysteresis index (A) calculated using the equation below[66] decreased from 0.34 (pristine $CsPbIBr_2$ device) to 0.21 (1% AgI $CsPbIBr_2$ device).

$$A = \frac{PCE(reverse\ scan) - PCE(forward\ scan)}{PCE(reverse\ scan)} \tag{2}$$

The 1% AgI $CsPbIBr_2$ PSC can have improved morphology with fewer grain boundaries with decreasing value of A, which can facilitate efficient charge carriers transport in the solar cell. Figure 4d shows the corresponding IPCE for the pristine and 1% AgI doped $CsPbIBr_2$ PSCs. The 1% AgI device exhibited higher IPCE over the entire wavelength range than the controlled device, which further corroborates the UV–vis results. The enhanced IPCE for the 1% AgI doped device can be attributed to compact and large grains, which consequently also enhanced charge extraction and suppressed charge recombination in the device.

The calculated *J*sc values are 11.06 mA/cm^2 and 11.83 mA/cm^2 for the pristine and 1% AgI-doped perovskite devices, respectively, match well with the experimental *J*sc values provided in Table 1. The slight variation may stem from the spectral mismatch between different solar simulators[67,68]. The box plot of 15 cells for the pristine and 1% AgI doped $CsPbIBr_2$ PSCs that present the statistical features of J_{sc}, *V*oc, *FF*, and PCE is shown in Fig. 5. The box plot indicates the enhancement of performance more. The average PV parameters of 1% AgI doped cells are higher than the control devices, and further confirms that Ag doping is beneficial in enhancing the PV parameters of $CsPbIBr_2$ PSC.

Hole-only devices with a geometry of FTO/PEDOT:PSS/$CsPbIBr_2$/P3HT/Ag, respectively, were fabricated in order to determine the trap state density (n_{trap}). Figure 6 shows the plots of *I–V* curves under dark conditions. The trap state density can be determined from the trap-filled limit voltage (V_{TFL}), according to the equation below[41,69].

$$n_{trap} = \frac{2\varepsilon\varepsilon_0}{ed^2} V_{TFL} \tag{3}$$

where ε is the relative dielectric constant of $CsPbIBr_2$, which is approximately equal to 8[22,70], ε_0 is the constant of vacuum permittivity in free space, d is the thickness of the perovskite film and e is the electron charge. V_{TFL} is estimated from the *I–V* curves. Table S1 shows the V_{TFL} and n_{trap} values of pristine and 1% AgI doped $CsPbIBr_2$ PSCs. The approximate V_{TFL} values for the hole only devices for the pristine and 1% AgI doped perovskite films were 0.159 V and 0.284 V, respectively. The n_{trap} for the hole-only devices for the pristine and 1% AgI doped $CsPbIBr_2$ perovskite films were calculated to be 4.02×10^{15} cm^{-3} and 2.25×10^{15} cm^{-3}, respectively (see Table S1). The defect densities for 1% AgI doped $CsPbIBr_2$ perovskite devices were reduced in comparison to the pristine devices. The decrease in defect density for the 1% AgI doped device is attributed to the high-quality perovskite film with enhanced crystallinity, enlarging grains, and fewer grain boundaries.

Conclusion

In summary, this paper reports improvement in the quality of $CsPbIBr_2$ perovskite films by incorporating AgI additive as an effective strategy. We studied the effects of AgI additive on the morphology, crystallinity, optical properties, and defect density of the $CsPbIBr_2$ perovskite films. Our investigation suggested that using the AgI additive in $CsPbIBr_2$ perovskite film has improved the structural, morphological, and optoelectronic properties of the perovskite films. The introduction of AgI in the $CsPbIBr_2$ precursor led to a uniform surface coverage of $CsPbIBr_2$ perovskite film that exhibited larger grain size, improved crystallinity, and decreased defect densities and carrier recombination. To confirm the effectiveness and effect of the AgI modified $CsPbIBr_2$ perovskite film on improving the PV properties of the solar cells. A simple planar structure was fabricated, and the 1% AgI device achieved a PCE of 7.20%, which is higher than the pristine device (5.2%). This work provides a useful strategy toward enhancing the film quality and optoelectronic properties of $CsPbIBr_2$ perovskites for the fabrication of efficient PSCs and other optoelectronic devices.

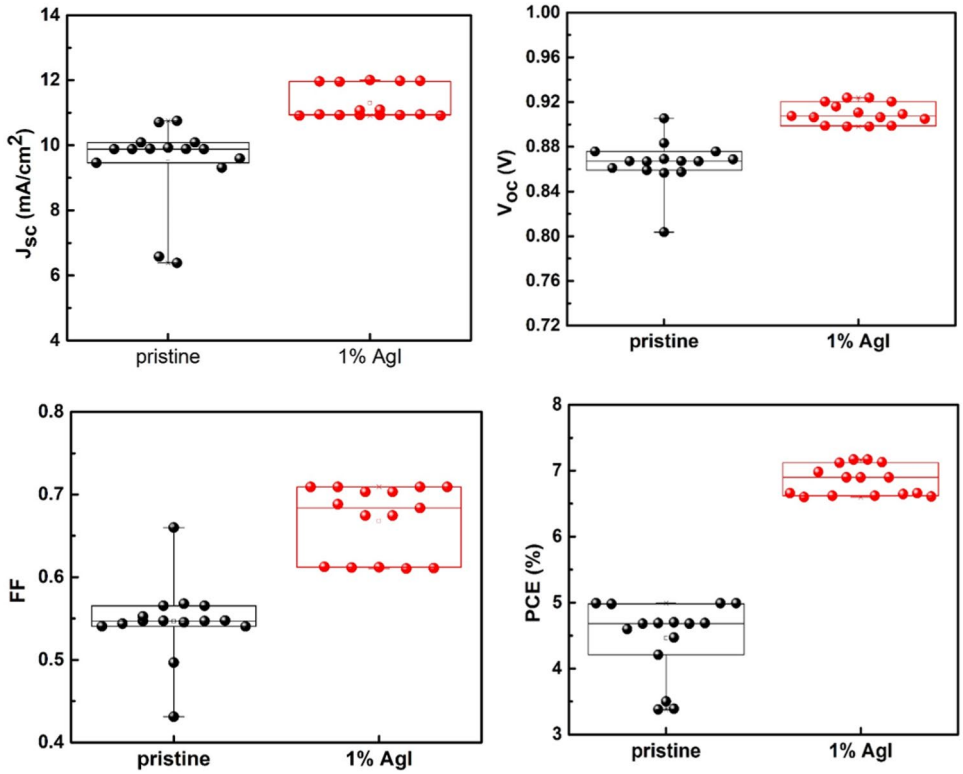

Figure 5. Statistical distribution of PV parameters for the pristine and AgI PSCs, based on 15 cells.

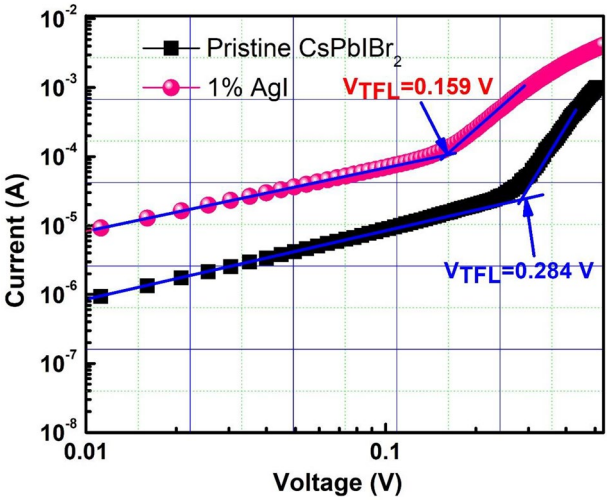

Figure 6. Hole-only devices films (FTO/PEDOT: PSS/CsPbIBr$_2$/P3HT/Ag) for pristine, and 1% AgI CsPbIBr$_2$ perovskite films.

Received: 20 October 2021; Accepted: 8 April 2022
Published online: 12 May 2022

References

1. Adams, G. R., Adhikari, N., Parker, H. & Okoli, O. Flexible wire-shaped perovskite photodetector via joule heating for improved crystallization and performance. *Adv. Mater. Interfaces* **5**, 1800082 (2018).
2. Kojima, A., Teshima, K., Shirai, Y. & Miyasaka, T. Organometal halide perovskites as visible-light sensitizers for photovoltaic cells. *J. Am. Chem. Soc.* **131**, 6050–6051 (2009).
3. Ling, Y. *et al.* Bright light-emitting diodes based on organometal halide perovskite nanoplatelets. *Adv. Mater.* **28**, 305–311 (2016).
4. Wang, X. *et al.* PIN diodes array made of perovskite single crystal for X-ray imaging. *Phys. Status Solidi (RRL) Rapid Res. Lett.* **12**, 1800380 (2018).

5. D'innocenzo, V. *et al.* Excitons versus free charges in organo-lead tri-halide perovskites. *Nat. Commun.* **5**, 3586 (2014).
6. Lee, M. M., Teuscher, J., Miyasaka, T., Murakami, T. N. & Snaith, H. J. Efficient hybrid solar cells based on meso-superstructured organometal halide perovskites. *Science* **338**, 643–647 (2012).
7. Stranks, S. D. *et al.* Electron-hole diffusion lengths exceeding 1 micrometer in an organometal trihalide perovskite absorber. *Science* **342**, 341–344 (2013).
8. Wehrenfennig, C., Eperon, G. E., Johnston, M. B., Snaith, H. J. & Herz, L. M. High charge carrier mobilities and lifetimes in organolead trihalide perovskites. *Adv. Mater.* **26**, 1584–1589 (2014).
9. Xing, G. *et al.* Long-range balanced electron-and hole-transport lengths in organic-inorganic $CH_3NH_3PbI_3$. *Science* **342**, 344–347 (2013).
10. The National Renewable Energy Laboratory. Best Research-Cell Efficiency Chart. https://www.nrel.gov/pv/cell-efficiency.html (2019).
11. Chen, L. *et al.* Inverted all-inorganic $CsPbI_2Br$ perovskite solar cells with promoted efficiency and stability by nickel incorporation. *Chem. Mater.* **31**, 9032–9039 (2019).
12. Jeon, N. J. *et al.* A fluorene-terminated hole-transporting material for highly efficient and stable perovskite solar cells. *Nat. Energy* **3**, 682 (2018).
13. Ono, L. K., Qi, Y. & Liu, S. F. Progress toward stable lead halide perovskite solar cells. *Joule* **2**, 1961–1990 (2018).
14. Rong, Y. *et al.* Challenges for commercializing perovskite solar cells. *Science* **361**, eaat8235 (2018).
15. Zhang, Q. *et al.* Light processing enables efficient carbon-based, all-inorganic planar $CsPbIBr_2$ solar cells with high photovoltages. *ACS Appl. Mater. Interfaces* **11**, 3 (2019).
16. Lau, C. F. J. *et al.* Strontium-doped low-temperature-processed $CsPbI_2Br$ perovskite solar cells. *ACS Energy Lett.* **2**, 2319–2325 (2017).
17. Saliba, M. *et al.* Incorporation of rubidium cations into perovskite solar cells improves photovoltaic performance. *Science* **354**, 206–209 (2016).
18. Saliba, M. *et al.* Cesium-containing triple cation perovskite solar cells: Improved stability, reproducibility and high efficiency. *Energy Environ. Sci.* **9**, 1989–1997 (2016).
19. Chen, W. *et al.* A semitransparent inorganic perovskite film for overcoming ultraviolet light instability of organic solar cells and achieving 14.03% efficiency. *Adv. Mater.* **30**, 1800855 (2018).
20. Duan, J., Zhao, Y., He, B. & Tang, Q. High-purity inorganic perovskite films for solar cells with 9.72% efficiency. *Angew. Chem.* **130**, 3849–3853 (2018).
21. Nam, J. K. *et al.* Potassium incorporation for enhanced performance and stability of fully inorganic cesium lead halide perovskite solar cells. *Nano Lett.* **17**, 2028–2033 (2017).
22. Eze, V. O., Adams, G. R., Braga Carani, L., Simpson, R. J. & Okoli, O. I. Enhanced inorganic $CsPbIBr_2$ perovskite film for a sensitive and rapid response self-powered photodetector. *J. Phys. Chem. C* **124**(38), 20643–20653 (2020).
23. Yin, G. *et al.* Precursor engineering for all-inorganic $CsPbI_2Br$ perovskite solar cells with 1478% efficiency. *Adv. Funct. Mater.* **28**, 1803269 (2018).
24. Zeng, Q. *et al.* Polymer-passivated inorganic cesium lead mixed-halide perovskites for stable and efficient solar cells with high open-circuit voltage over 1.3 V. *Adv. Mater.* **30**, 1705393 (2018).
25. Zhu, W. *et al.* Intermolecular exchange boosts efficiency of air-stable, carbon-based all-inorganic planar $CsPbIBr_2$ perovskite solar cells to over 9%. *Adv. Energy Mater.* **8**, 1802080 (2018).
26. Liang, J. *et al.* All-inorganic perovskite solar cells. *J. Am. Chem. Soc.* **138**, 15829–15832 (2016).
27. Duan, J., Zhao, Y., He, B. & Tang, Q. High-purity inorganic perovskite films for solar cells with 9.72% efficiency. *Angew. Chem. Int. Ed.* **57**, 3787–3791 (2018).
28. Subhani, W. S., Wang, K., Du, M. & Liu, S. F. Goldschmidt-rule-deviated perovskite $CsPbIBr_2$ by barium substitution for efficient solar cells. *Nano Energy* **61**, 165–172 (2019).
29. Wu, Y. *et al.* Thermally stable $MAPbI_3$ perovskite solar cells with efficiency of 19.19% and area over 1 cm^2 achieved by additive engineering. *Adv. Mater.* **29**, 1701073 (2017).
30. Liang, J. *et al.* Enhancing optical, electronic, crystalline, and morphological properties of cesium lead halide by Mn substitution for high-stability all-inorganic perovskite solar cells with carbon electrodes. *Adv. Energy Mater.* **8**, 1800504 (2018).
31. Liu, W. *et al.* Mn^{2+}-doped lead halide perovskite nanocrystals with dual-color emission controlled by halide content. *J. Am. Chem. Soc.* **138**, 14954–14961 (2016).
32. Parobek, D. *et al.* Exciton-to-dopant energy transfer in Mn-doped cesium lead halide perovskite nanocrystals. *Nano Lett.* **16**, 7376–7380 (2016).
33. Van der Stam, W. *et al.* Highly emissive divalent-ion-doped colloidal $CsPb_{1-x}M_xBr_3$ perovskite nanocrystals through cation exchange. *J. Am. Chem. Soc.* **139**, 4087–4097 (2017).
34. Zhou, S. *et al.* Ag-doped halide perovskite nanocrystals for tunable band structure and efficient charge transport. *ACS Energy Lett.* **4**, 534–541 (2019).
35. Bai, D. *et al.* Interstitial Mn^{2+}-driven high-aspect-ratio grain growth for low-trap-density microcrystalline films for record efficiency $CsPbI_2Br$ solar cells. *ACS Energy Lett.* **3**, 970–978 (2018).
36. Hu, Y. *et al.* Bismuth incorporation stabilized α-$CsPbI_3$ for fully inorganic perovskite solar cells. *ACS Energy Lett.* **2**, 2219–2227 (2017).
37. Tan, X. *et al.* Enhancing the optical, morphological and electronic properties of the solution-processed $CsPbIBr_2$ films by Li doping for efficient carbon-based perovskite solar cells. *Appl. Surf. Sci.* **499**, 143990 (2020).
38. Sun, H. *et al.* Pb-reduced $CsPb_{0.9}Zn_{0.1}I2Br$ thin films for efficient perovskite solar cells. *Adv. Energy Mater.* **9**, 1900896 (2019).
39. Xiang, W. *et al.* Europium-doped $CsPbI_2Br$ for stable and highly efficient inorganic perovskite solar cells. *Joule* **3**, 205–214 (2019).
40. Liang, J. *et al.* $CsPb_{0.9}Sn_{0.1}IBr_2$ based all-inorganic perovskite solar cells with exceptional efficiency and stability. *J. Am. Chem. Soc.* **139**, 14009–14012 (2017).
41. Guo, Y., Yin, X., Liu, J. & Que, W. Highly efficient $CsPbIBr_2$ perovskite solar cells with efficiency over 9.8% using preheating-assisted spin-coating method. *J. Mater. Chem. A* **7**, 19008–19016 (2019).
42. Wang, Z., Baranwal, A. K., Pandey, M., Ma, T. & Hayase, S. Xanthate-induced sulfur doped all-inorganic perovskite with superior phase stability and enhanced performance. *Nano Energy* **59**, 258–267 (2019).
43. Liu, C. *et al.* Ultra-thin MoO_x as cathode buffer layer for the improvement of all-inorganic $CsPbIBr_2$ perovskite solar cells. *Nano Energy* **41**, 75–83 (2017).
44. Shahbazi, S. *et al.* Ag doping of organometal lead halide perovskites: Morphology modification and p-type character. *J. Phys. Chem. C* **121**, 3673–3679 (2017).
45. Eze, V. O., Lei, B. & Mori, T. Air-assisted flow and two-step spin-coating for highly efficient $CH_3NH_3PbI_3$ perovskite solar cells. *Jpn. J. Appl. Phys.* **55**, 02BF08 (2016).
46. Eze, V. O. & Mori, T. Enhanced photovoltaic performance of planar perovskite solar cells fabricated in ambient air by solvent annealing treatment method. *Jpn J. Appl. Phys.* **55**, 122301 (2016).
47. Eze, V. O., Seike, Y. & Mori, T. Efficient planar perovskite solar cells using solution-processed amorphous WO_x/fullerene C60 as electron extraction layers. *Org. Electron.* **46**, 253–262 (2017).

48. Li, X. *et al.* Amorphous nanoporous WO_x modification for stability enhancement and hysteresis reduction in TiO_2-based perovskite solar cells. *Sol. Energy Mater. Sol. Cells* **196**, 157–166 (2019).
49. Eze, V. O., Seike, Y. & Mori, T. Synergistic effect of additive and solvent vapor annealing on the enhancement of $MAPbI_3$ perovskite solar cells fabricated in ambient air. *ACS Appl. Mater. Interfaces* **12**, 41 (2020).
50. Chen, Q. *et al.* Ag-incorporated organic–inorganic perovskite films and planar heterojunction solar cells. *Nano Lett.* **17**, 3231–3237 (2017).
51. Kato, Y. *et al.* Silver iodide formation in methyl ammonium lead iodide perovskite solar cells with silver top electrodes. *Adv. Mater. Interfaces* **2**, 1500195 (2015).
52. Siegler, T. D. *et al.* Addition of monovalent silver cations to $CH_3NH_3PbBr_3$ produces crystallographically oriented perovskite thin films. *ACS Appl. Energy Mater.* **2**(8), 6087–6096 (2019).
53. Navas, J. *et al.* New insights into organic–inorganic hybrid perovskite $CH_3NH_3PbI_3$ nanoparticles. An experimental and theoretical study of doping in Pb^{2+} sites with Sn^{2+}, Sr^{2+}, Cd^{2+} and Ca^{2+}. *Nanoscale* **7**, 6216–6229 (2015).
54. Fan, L. *et al.* Unusually dispersed AgI quantum dots for efficient HTL-free $CH_3NH_3PbI_3$ photovoltaics. *ACS Appl. Mater. Interfaces* **11**, 45568–45577 (2019).
55. Lei, B., Eze, V. O. & Mori, T. High-performance $CH_3NH_3PbI_3$ perovskite solar cells fabricated under ambient conditions with high relative humidity. *Jpn J. Appl. Phys.* **54**, 100305 (2015).
56. Lei, B., Eze, V. O. & Mori, T. Effect of morphology control of light absorbing layer on $CH_3NH_3PbI_3$ perovskite solar cells. *J. Nanosci. Nanotechnol.* **16**, 3176–3182 (2016).
57. Wang, K. *et al.* High-performance simple-structured planar heterojunction perovskite solar cells achieved by precursor optimization. *ACS Omega* **2**, 6250–6258 (2017).
58. Geske, T. *et al.* Deterministic nucleation for halide perovskite thin films with large and uniform grains. *Adv. Funct. Mater.* **27**, 1702180 (2017).
59. Eperon, G. E., Burlakov, V. M., Docampo, P., Goriely, A. & Snaith, H. J. Morphological control for high performance, solution-processed planar heterojunction perovskite solar cells. *Adv. Funct. Mater.* **24**, 151–157 (2014).
60. Zhang, P. *et al.* Preparation of perovskite films under liquid nitrogen atmosphere for high efficiency perovskite solar cells. *ACS Sustain. Chem. Eng.* **7**, 3956–3961 (2019).
61. Eames, C. *et al.* Ionic transport in hybrid lead iodide perovskite solar cells. *Nat. Commun.* **6**, 1–8 (2015).
62. Kim, H.-S. & Park, N.-G. Parameters affecting I-V hysteresis of $CH_3NH_3PbI_3$ perovskite solar cells: effects of perovskite crystal size and mesoporous TiO_2 layer. *J. Phys. Chem. Lett.* **5**, 2927–2934 (2014).
63. Snaith, H. J. *et al.* Anomalous hysteresis in perovskite solar cells. *J. Phys. Chem. Lett.* **5**, 1511–1515 (2014).
64. Xiao, Z. *et al.* Giant switchable photovoltaic effect in organometal trihalide perovskite devices. *Nat. Mater.* **14**, 193–198 (2015).
65. Zhang, Y. *et al.* Charge selective contacts, mobile ions and anomalous hysteresis in organic–inorganic perovskite solar cells. *Mater. Horiz.* **2**, 315–322 (2015).
66. Habisreutinger, S. N., Noel, N. K. & Snaith, H. J. Hysteresis index: A figure without merit for quantifying hysteresis in perovskite solar cells. *ACS Energy Lett.* **3**, 2472–2476 (2018).
67. Yang, S. *et al.* Excellent moisture stability and efficiency of inverted all-inorganic $CsPbIBr_2$ perovskite solar cells through molecule interface engineering. *ACS Appl. Mater. Interfaces* **12**, 13931–13940 (2020).
68. Zhu, W. *et al.* Interfacial voids trigger carbon-based, all-inorganic $CsPbIBr_2$ perovskite solar cells with photovoltage exceeding 1.33 V. *Nano-Micro Lett.* **12**, 1–14 (2020).
69. Jiang, L. L. *et al.* Passivated perovskite crystallization via g-C_3N_4 for high-performance solar cells. *Adv. Funct. Mater.* **28**, 1705875 (2018).
70. Yang, Z. *et al.* Unraveling the exciton binding energy and the dielectric constant in single-crystal methylammonium lead triiodide perovskite. *J. Phys. Chem. Lett.* **8**, 1851–1855 (2017).

Acknowledgements

The authors thank Dr. Seigriest for the XRD measurements. The funding for this work was provided by the NSF Award Nos. 1359235 and NSF/DMR-1644779. MJU acknowledge the fund provided by DoE Award No. DE-NA0004004.

Author contributions

Methodology and original draft preparation were done by V.O.E. and L.B.C. Writing—review and editing was done by V.O.E. and H.M. Formal analysis was done by V.O.E., L.B.C. and H.M. Investigation was done by V.O.E., L.B.C, O.I.O., M.J.U. Data curation was done by V.O.E. Validation was done by V.O.E., L.B.C, O.I.O., H.M., M.J.U. Conceptualization was done by V.O.E., O.I.O., M.J.U. Project administration, supervision, and funding acquisition was done by O.I.O., M.J.U. All authors reviewed the manuscript.

Competing interests

The authors declare no competing interests.

Additional information

Supplementary Information The online version contains supplementary material available at https://doi.org/10.1038/s41598-022-11729-0.

Correspondence and requests for materials should be addressed to M.J.U. or O.I.O.

Reprints and permissions information is available at www.nature.com/reprints.

Publisher's note Springer Nature remains neutral with regard to jurisdictional claims in published maps and institutional affiliations.